New Journal of Physics
The open access journal at the forefront of physics

Deutsche Physikalische Gesellschaft DPG
IOP Institute of Physics

Published in partnership with: Deutsche Physikalische Gesellschaft and the Institute of Physics

OPEN ACCESS

RECEIVED
21 August 2018

REVISED
14 November 2018

ACCEPTED FOR PUBLICATION
23 November 2018

PUBLISHED
14 December 2018

PAPER

Quantum optimal control of the dissipative production of a maximally entangled state

Karl P Horn[1], Florentin Reiter[2], Yiheng Lin[3,4], Dietrich Leibfried[5] and Christiane P Koch[1]

[1] Theoretische Physik, Universität Kassel, Heinrich-Plett-Straße 40, D-34132 Kassel, Germany
[2] Department of Physics, Harvard University, Cambridge, MA 02138, United States of America
[3] CAS Key Laboratory of Microscale Magnetic Resonance and Department of Modern Physics, University of Science and Technology of China, Hefei 230026, People's Republic of China
[4] Synergetic Innovation Center of Quantum Information and Quantum Physics, University of Science and Technology of China, Hefei 230026, People's Republic of China
[5] National Institute of Standards and Technology, Boulder, CO 80305, United States of America

E-mail: christiane.koch@uni-kassel.de

Keywords: quantum optimal control, entanglement, trapped ions, quantum reservoir engineering, open quantum systems

Abstract

Entanglement generation can be robust against certain types of noise in approaches that deliberately incorporate dissipation into the system dynamics. The presence of additional dissipation channels may, however, limit fidelity and speed of the process. Here we show how quantum optimal control techniques can be used to both speed up the entanglement generation and increase the fidelity in a realistic setup, whilst respecting typical experimental limitations. For the example of entangling two trapped ion qubits (Lin *et al* 2013 *Nature* **504** 415), we find an improved fidelity by simply optimizing the polarization of the laser beams utilized in the experiment. More significantly, an alternate combination of transitions between internal states of the ions, when combined with optimized polarization, enables faster entanglement and decreases the error by an order of magnitude.

1. Introduction

Quantum devices aim to exploit the two essential elements of quantum physics, quantum coherence and entanglement, for practical applications. They require the implementation of a number of basic tasks such as state preparation or generation of entanglement, all the while preserving the relevant non-classical features at the level of device operation. The implementation of quantum tasks thus needs to be robust with respect to parameter fluctuations and external noise that is unavoidable in any real physical setup.

Loss of coherence and noise are commonly attributed to the coupling of the quantum system with its surrounding environment [1]. One strategy for realizing all necessary tasks with sufficient accuracy is to perform the quantum operations at a time scale faster than the time scale at which the noise affects the system. Quantum optimal control theory provides a set of tools to derive the corresponding protocols [2] and can be used to identify the quantum speed limit [3–6], i.e. the shortest possible duration within which the operation can be carried out with a pre-specified fidelity.

Nevertheless, there is a fundamental limit in that one cannot 'beat' the noise, particularly, when its time scales are comparable to or faster than the typical speed limits of the target operation. An alternative is found in approaches that deliberately incorporate dissipation into the system dynamics, often referred to as quantum reservoir engineering [7]. The basic idea is to implement stochastic dynamics whose stationary state is non-classical. This is achieved by manipulating the coupling to the environment, or reservoir. In its simplest form, a constant but switchable coupling is realized by an electromagnetic field that drives a transition to a state with fast decay [7]. The dynamics are described by the quantum optical master equation [1], and the system will eventually be driven into the fixed point of the corresponding Liouvillian [8, 9].

Applications of this basic idea are many faceted—its use has been suggested, for example in generating entanglement [10–23], implementing universal quantum computing [9], driving phase transitions [24–26] and

autonomous quantum error correction [27–29]. Experimentally, the generation of non-classical states [30], entangled states [31–34], and non-equilibrium quantum phases [35–37] have successfully been demonstrated. Engineered dissipation can also be used towards a better understanding of open quantum system dynamics, by means of quantum simulation [37].

All of these examples testify to the fact that dissipation can be a resource [9] for quantum technology. The ultimate performance bounds that can be reached with driven-dissipative dynamics under realistic conditions have, however, not yet been explored. While quantum reservoir engineering has been advocated for its robustness, its performance in a practical setting is compromised as soon as additional noise sources perturb the steady state or trap population flowing towards it.

This can be illustrated by examining the experiment described in [32]. For a $^{9}Be^{+} - {}^{24}Mg^{+} - {}^{24}Mg^{+} - {}^{9}Be^{+}$ chain occupying the same linear Paul trap, the two $^{9}Be^{+}$ ions were entangled via their collective motion using hyperfine electronic ground state levels as logical states. Entanglement was achieved by applying a combination of laser and microwave transitions. This could be done in an either time-continuous manner or by repeating a fixed sequence of steps, driving the system into a steady state, with the majority of population in the targeted, maximally entangled singlet state. Desired dissipation was brought into play by a combination of spin-motion coupling from a sideband laser, motion dissipation by sympathetically cooling cotrapped $^{24}Mg^{+}$ ions, and a repump laser which addresses the transition to a rapidly decaying electronically excited state. The sideband laser beams also lead to undesired pumping of spins, so-called spontaneous emission. This resulted in population leakage and was the main source of error in that experiment [32].

The simultaneous presence of both desired and undesired dissipation channels is rather generic. To harness the full power of dissipative entangled state preparation, one would like to exploit the former while mitigating the latter. Here, we use quantum optimal control theory [2] to address this problem. For the example of preparing two trapped ions in a maximally entangled state [32], we ask whether entanglement can be generated faster and more accurately when judiciously choosing a few key parameters. In order to keep in line with the experimental setup described in [32], we forego the usual assumption of time-dependent pulses whose shapes are derived by quantum optimal control. Instead, we employ electromagnetic fields with constant amplitude and use tools from nonlinear optimization to directly determine the best field strengths, detunings and polarizations. Our approach allows to not only determine the optimal values for these parameters, but also, identify key factors that ultimately limit fidelity and speed of entanglement generation. Based on this insight, we explore an alternative set of transitions and show that this scheme can outperform the original one both in terms of fidelity and speed.

The paper is organized as follows. Section 2 recalls the mechanism for entanglement generation in the experiment of [32] and details the theoretical description of the corresponding trapped ion system. Optimization of the transitions used in [32] is discussed in section 3. An alternative set of transitions is introduced in section 4, together with the optimization of the corresponding experimental parameters. We conclude in section 5.

2. Model

In this section we consider the system described in [32], consisting of a linear Paul trap containing $^{9}Be^{+}$ ions and $^{24}Mg^{+}$ ions, which interact mutually through their Coulomb repulsion and with external electric fields. A unitary idealization of these interactions is summarized in the Hamiltonian H. The mechanism giving rise to dissipation in the state preparation process is spontaneous emission after excitation of internal electronic states of the ion by the external laser fields. The system dynamics is therefore described by the quantum optical master equation in Lindblad form (with $\hbar = 1$),

$$\partial_t \rho = \mathcal{L}\rho = -\mathrm{i}[H, \rho] + \mathcal{L}_{\mathcal{D}}\rho. \tag{1}$$

We refer to $\mathcal{L}_{\mathcal{D}}$ as the (Lindblad) dissipator, which is given by

$$\mathcal{L}_{\mathcal{D}}\rho = \sum_k \left(L_k \rho L_k^{\dagger} - \frac{1}{2}[L_k^{\dagger} L_k, \rho] \right), \tag{2}$$

where the sum over k contains individual contributions due to sympathetic cooling, heating and photon scattering occurring during stimulated Raman processes and repumping into an electronically excited state.

2.1. State space

The model Hamiltonian H accounts for the internal structure of two $^{9}Be^{+}$ ions as well as two vibrational modes of the trapped ion chain. The state space of the considered system consists of the following tensor product structure

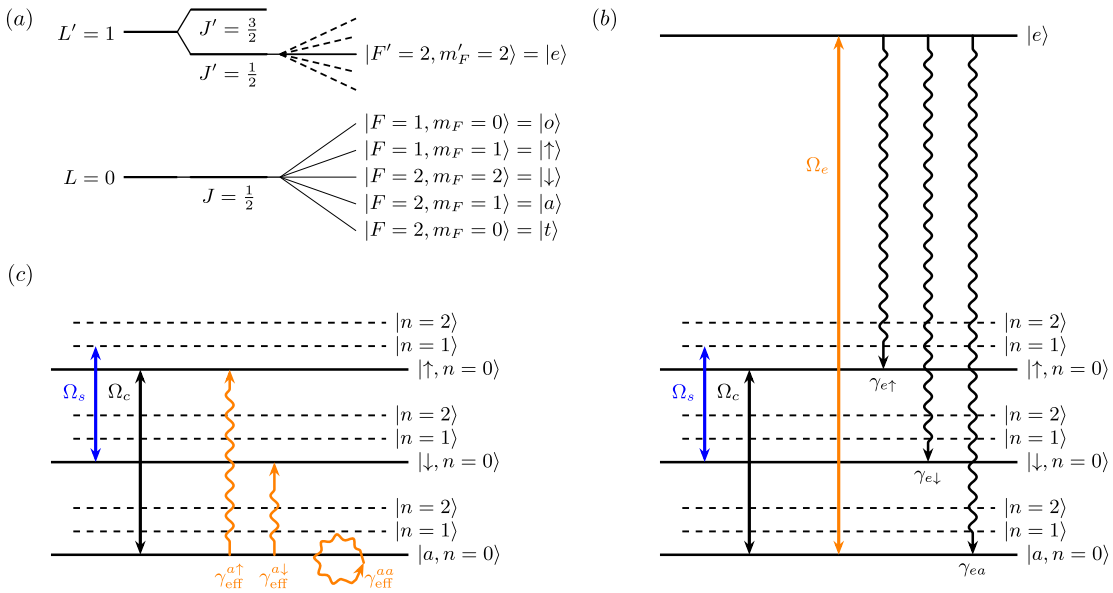

Figure 1. (a) The fine and hyperfine structure of the electronic ground and first excited state of $^9Be^+$, including the most relevant hyperfine levels. (b) In the original scheme [32], a stimulated Raman blue sideband transition from the $|\downarrow\rangle$ to the $|\uparrow\rangle$ level (Ω_s), represented by a blue double-headed arrow, a microwave carrier transition between the $|a\rangle$ and $|\uparrow\rangle$ levels (Ω_c), represented by a black double-headed arrow, and a repump transition out of $|a\rangle$ into the excited level $|e\rangle$ (Ω_e), represented by an orange double-headed arrow, are driven. $|e\rangle$ rapidly decays back into $|a\rangle$, $|\downarrow\rangle$ and $|\uparrow\rangle$, as represented by the black snaking lines. (c) In the picture after adiabatic elimination [32], the excited level $|e\rangle$ no longer explicitly appears and effective decay, represented by orange snaking lines, occurs directly out of $|a\rangle$. In (b) and (c), n refers to the occupation number of the utilized vibrational mode.

$$(n_{\text{qb1}}) \otimes (n_{\text{qb2}}) \otimes (n_{\nu_1}) \otimes (n_{\nu_2}). \tag{3}$$

In equation (3) n_{qb1} and n_{qb2} designate hyperfine states of the $^9Be^+$ ions, specified by the quantum numbers F and their projections m_F, obtained from coupling the total electronic angular momentum quantum number J with the nuclear spin quantum number I. Figure 1(a) highlights the hyperfine states of interest, comprising of $|\downarrow\rangle \stackrel{\text{def}}{=} |S_{1/2},\ F = 2,\ m_F = 2\rangle$ and $|\uparrow\rangle \stackrel{\text{def}}{=} |S_{1/2},\ F = 1,\ m_F = 1\rangle$, the two hyperfine levels to entangle, as well as an auxiliary level $|a\rangle \stackrel{\text{def}}{=} |S_{1/2},\ F = 2,\ m_F = 1\rangle$. The neighboring levels $|o\rangle \stackrel{\text{def}}{=} |S_{1/2},\ F = 1,\ m_F = 0\rangle$ and $|t\rangle \stackrel{\text{def}}{=} |S_{1/2},\ F = 2,\ m_F = 0\rangle$ are also accounted for in the model, since these are predominantly populated by inadvertent scattering processes. In the following, the onlyelectronically excited state of interest will be $|e\rangle \stackrel{\text{def}}{=} |P_{1/2},\ F' = 2,\ m'_F = 2\rangle$.

n_{ν_1} and n_{ν_2} are vibrational quantum numbers of two of the four shared motional modes of the trapped ionic crystal along its linear axis. Entanglement generation employs ν_1, and sideband transitions utilizing this mode are essential for the presented schemes. Unless specifically required, the mode ν_2, which is not utilized for entanglement but is included in the model to account for off-resonant coupling, will be suppressed notationally for the sake of simplicity. It is assumed that the trap has an axis of weakest confinement along which the four-ion string is aligned and that the eight radial motional modes can be neglected, since they are largely decoupled given the sideband laser configuration described in [32]. Figure 1(b) shows three transitions that were driven on a single $^9Be^+$ ion in [32]. These belong to the coherent part of equation (1), described by H, and one of them results in population of the electronically excited state $|e\rangle$ with subsequent dissipation which is modeled by the incoherent part, $\mathcal{L}_{\mathcal{D}}\rho$. After adiabatic elimination, however, the transition to $|e\rangle$ no longer appears in the coherent part of equation (1), while the dissipative part is modified by the result of the adiabatic elimination to fully account for the effective decay out of a electronic ground state hyperfine level instead [32]. This is illustrated in figure 1(c).

2.2. Original scheme for entanglement preparation

As represented in figure 1, the dissipative entanglement generation of [32] uses three different types of fields to induce population flow in the state space. The entanglement mechanism can be understood by qualitatively tracing the flow of population from state to state as indicated in figure 2. Entangling the two $^9Be^+$ ions via their joint motion in the trap is made possible by utilizing sideband transitions driven by Raman lasers. These change the internal states of the $^9Be^+$ ions whilst simultaneously exciting or de-exciting the utilized motional mode. In contrast, carrier transitions driven by a microwave field change the $^9Be^+$ internal states only. Finally, a repump laser excites population to a short-lived electronically excited state. Specifically, in [32], a single sideband

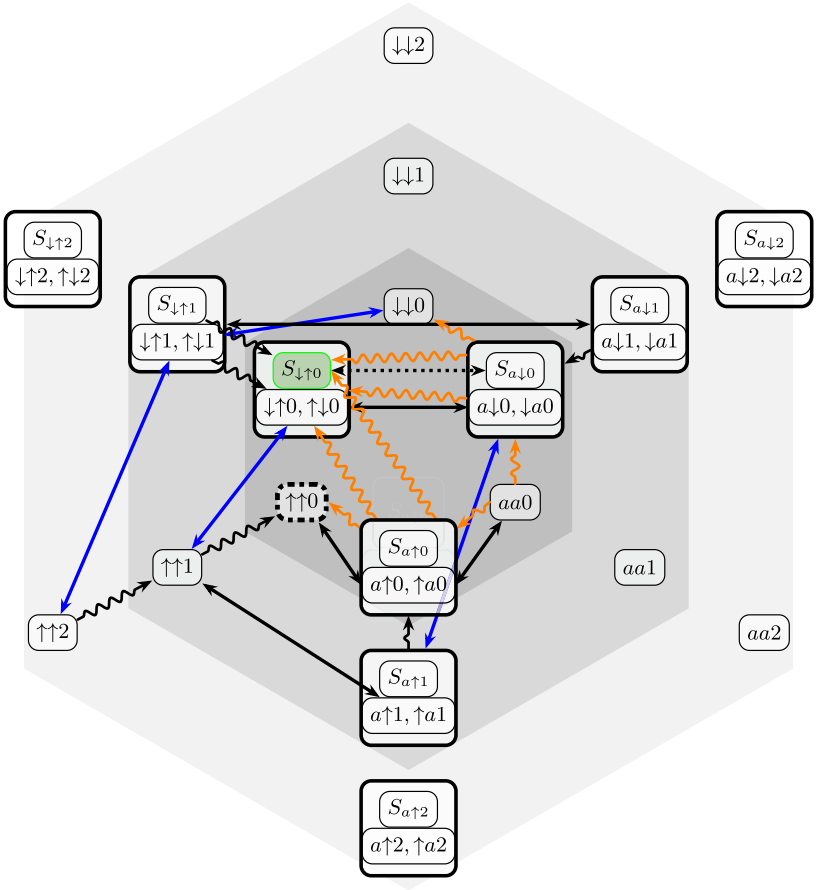

Figure 2. Graphical overview of transitions needed for steady state entanglement. For simplicity, only states within the hyperfine subspace $\{a, \downarrow, \uparrow\}$ and only the mode ν_1 are displayed. The vibrational quantum number of the utilized mode increases radially outwards from the center with shaded areas sharing the same quantum number. Carrier transitions between $|a\rangle$ and $|\uparrow\rangle$ at rate $\Omega_{\mathrm{car},a,\uparrow}$ are represented by black double headed arrows. Sideband transitions between $|\downarrow\rangle$ and $|\uparrow\rangle$ at rate $\Omega^{2p}_{\mathrm{blue},\downarrow,\uparrow}$ are represented by blue double headed arrows. Effective decay from $|a\rangle$ at the rates $\gamma^{\mathrm{eff}}_{a,f}$ for $f \in \{a, \downarrow, \uparrow\}$, is represented by orange snaking lines. Sympathetic cooling of the utilized vibrational mode is represented by black snaking lines, whilst heating acts in the opposite direction and is not shown. For the sake of clarity, certain transitions are omitted and the leaking between the hyperfine states is also not shown.

transition between $|\downarrow\rangle$ and $|\uparrow\rangle$, a carrier transition between $|a\rangle$ and $|\uparrow\rangle$ and a repump transition between $|a\rangle$ and $|e\rangle$ are used. Figure 1 indicates the transitions between the hyperfine levels of interest for a single $^9Be^+$ ion. The above transitions can be driven simultaneously and time-independently for the duration of the experiment or in a step-wise manner [32]. Here, we focus on the continuous case, which resulted in a larger error. Each $^9Be^+$ ion is affected by the driven transitions independently and no individual addressing is required. Starting with both $^9Be^+$ ions in an arbitrary state confined to the hyperfine subspace $\{a, \downarrow, \uparrow\}$, in the ideal case, this scheme always leads to a steady state in which the the population is trapped in the singlet entangled state between $|\downarrow\rangle$ and $|\uparrow\rangle$, $|S_{\downarrow\uparrow}\rangle \stackrel{\mathrm{def}}{=} \frac{1}{\sqrt{2}}(|\downarrow\uparrow\rangle - |\uparrow\downarrow\rangle)$. In the following, all singlet entangled states are designated by $|S_{ij}\rangle \stackrel{\mathrm{def}}{=} \frac{1}{\sqrt{2}}(|ij\rangle - |ji\rangle)$, whilst the triplet entangled states are designated by $|T_{ij}\rangle \stackrel{\mathrm{def}}{=} \frac{1}{\sqrt{2}}(|ij\rangle + |ji\rangle)$, $\forall\, i, j \in \{a, \downarrow, \uparrow\}$.

Let us inspect in more detail the flow of population from state to state in figure 2. Starting in $|\downarrow\downarrow\, n_{\nu_1} = 0\rangle$, for instance, it is possible to reach the target singlet entangled state $|S_{\downarrow\uparrow}\rangle$ by two sideband transitions leading to $|\uparrow\uparrow\, n_{\nu_1}\rangle$, followed by a carrier transition into a combination of the $|a\uparrow\, n_{\nu_1}\rangle$ and $|\uparrow an_{\nu_1}\rangle$ states. Population in the auxiliary state is driven by the repump laser into the electronically excited state from where it subsequently decays back into the electronic ground state hyperfine subspace. The process of electronic excitation and decay happens sufficiently fast with respect to the other transitions, that it can be regarded as 'effective decay' directly out of $|a\rangle$, as depicted in figures 1(b) and (c). This decay drives the system into a combination of $|\uparrow\uparrow\, n_{\nu_1}\rangle$, the triplet entangled state $|T_{\downarrow\uparrow}\rangle \otimes |n_{\nu_1}\rangle$, and the target state $|S_{\downarrow\uparrow}\rangle \otimes |n_{\nu_1}\rangle$. At any stage, sympathetic cooling can counteract the excitations of the vibrational mode in the trap which are caused by sideband transitions and heating. Sympathetic cooling is induced by a different set of sideband lasers driving transitions only between internal states of the $^{24}Mg^+$ ions which share common motional modes with the $^9Be^+$ ions. The carrier

transition between $|a\rangle$ and $|\uparrow\rangle$ leads out of the target state $|S_{\downarrow\uparrow}\rangle$ into $|S_{a\downarrow}\rangle$. This particular transition is highlighted specifically in figure 2 by a dotted black double headed arrow.

By ensuring that the two-photon Rabi frequency $\Omega^{2p}_{\text{blue},\downarrow,\uparrow}$ of the stimulated Raman sideband transition between $|\downarrow\rangle$ and $|\uparrow\rangle$ is much larger than the carrier Rabi frequency $\Omega_{\text{car},a,\uparrow}$, the latter transition can effectively be suppressed. Figure 2 also highlights the state $|\uparrow\uparrow\ 0\rangle$ with a thick, dotted, black border, since the effective decay, proportional to the square of the repump laser Rabi frequency $\Omega_{\text{car},a,e}$ must be made sufficiently weak relative to $\Omega_{\text{car},a,\uparrow}$, in order to prevent the trapping of population in $|\uparrow\uparrow\ 0\rangle$. Consequently, a hierarchy of rates is established in which the maximum attainable two-photon Rabi frequency of the stimulated Raman transition determines the maximal carrier Rabi frequency between $|a\rangle$ and $|\uparrow\rangle$, which in turn determines the maximal repump Rabi frequency between $|a\rangle$ and $|e\rangle$.

2.3. Hamiltonian

In the rotating wave approximation and interaction picture, the total system Hamiltonian is comprised of the driven hyperfine transitions

$$H = \sum_{\text{type},i,f} H_{\text{type},i,f}, \tag{4}$$

where the sum runs over specific triples (type, i, f), designating a transition of type 'red' or 'blue' sideband or 'carrier', between the initial and final hyperfine states $|i\rangle$ and $|f\rangle$.

Transitions of the carrier type between the ground state hyperfine levels are driven by microwave fields with a Hamiltonian of the form

$$\begin{aligned} H_{\text{car},i,f} = \Omega_{\text{car},i,f}(|f\rangle\langle i| \otimes \mathbb{1}_{\text{qb2}} \otimes \mathbb{1}_{\nu_1} \otimes \mathbb{1}_{\nu_2} \\ + \mathbb{1}_{\text{qb1}} \otimes |f\rangle\langle i| \otimes \mathbb{1}_{\nu_1} \otimes \mathbb{1}_{\nu_2}) e^{-i\Delta_{\text{car},i,f}t} + \text{h.c.}. \end{aligned} \tag{5}$$

Above, $\Omega_{\text{car},i,f}$ denotes the Rabi frequency and $\Delta_{\text{car},i,f}$ a small detuning between the applied field and the transition energy between $|i\rangle$ and $|f\rangle$. Each identity operator $\mathbb{1}_j$, with $j \in \{\text{qb1}, \text{qb2}, \nu_1, \nu_2\}$, is labeled according to the subspace to which it corresponds. A repump laser is required to drive transitions between ground and electronically excited hyperfine states. These transitions therefore involve Hamiltonians of the form of equation (5), where $|i\rangle$ is a hyperfine ground state level and $|f\rangle = |e\rangle$ is the addressed electronically excited hyperfine level. Since population excited by this repumper decays very rapidly into the hyperfine ground states, adiabatically eliminating the excited state is well justified.

Ideally, a blue sideband transition between two hyperfine levels $|i\rangle$ and $|f\rangle$, utilizing the motional mode ν_1, is represented by

$$\begin{aligned} H_{\text{blue},i,f} = \Omega_{\text{blue},i,f}(|f\rangle\langle i| \otimes \mathbb{1}_{\text{qb2}} \otimes b^+ \otimes \mathbb{1}_{\nu_2} \\ + \mathbb{1}_{\text{qb1}} \otimes |f\rangle\langle i| \otimes b^+ \otimes \mathbb{1}_{\nu_2}) e^{-i\Delta_{\text{blue},i,f}t} + \text{h.c.}, \end{aligned} \tag{6}$$

where $\Omega_{\text{blue},i,f}$ is the sideband Rabi frequency and $\Delta_{\text{blue},i,f}$ a small detuning from the energy difference between $|i\rangle$ and $|f\rangle$ plus the energy of one quantum of ν_1. b^+ and b denote the bosonic creation and annihilation operators which respectively excite and de-excite the harmonic mode ν_1. Analogously, the Hamiltonian of a red sideband transition takes the form of equation (6) but with the annihilation operator b replacing the creation operators $b^\dagger$ and $\Delta_{\text{blue},i,f}$ replaced by $\Delta_{\text{red},i,f}$.

In the specific case of a stimulated Raman sideband transition, $\Omega_{\text{red/blue},i,f}$ in equation (6) becomes $\Omega^{2p}_{\text{red/blue},i,f}$, a two-photon Rabi frequency of a red/blue sideband transition between $|i\rangle$ and $|f\rangle$, given by

$$\Omega^{2p}_{\text{red/blue},i,f} = \eta_{\nu_1}\frac{\mu^2 E_r E_b}{4}\sum_k \frac{\langle f|d\cdot\varepsilon_r|k\rangle\langle k|d\cdot\varepsilon_b|i\rangle}{\Delta_k \mu^2}. \tag{7}$$

In the following we assume Lamb–Dicke parameters of $\eta_{\nu_1} = 0.180$ and $\eta_{\nu_2} = 0.155$ for the utilized (ν_1) and off-resonant (ν_2) motional modes, respectively [32]. Above, E_r and E_b are the field strengths of the lower (red) and higher (blue) frequency Raman laser beams which have polarizations ε_r and ε_b, expressed in spherical components as $\varepsilon_r = (r_-, r_0, r_+)$ and $\varepsilon_b = (b_-, b_0, b_+)$, respectively. d is the dipole operator for the $^9Be^+$ ions (also expressed in the spherical basis) and the sum runs over all hyperfine levels $|k\rangle$ in the electronically excited states $P_{1/2}$ and $P_{3/2}$. The laser frequencies are shifted, such that the ground state to excited state transitions are detuned by Δ_e and $\Delta_e + f_P$ below the $S_{1/2} \leftrightarrow P_{1/2}$ and $S_{1/2} \leftrightarrow P_{3/2}$ resonances, respectively. $f_P \approx 197.2$ GHz is the fine structure splitting between $P_{1/2}$ and $P_{3/2}$. For the detuning between $|i\rangle$ and an individual excited state hyperfine level $|k\rangle$, the hyperfine splitting is neglected such that

$$\Delta_k \approx \begin{cases} \Delta_e, & \text{if } |k\rangle \in P_{1/2} \\ \Delta_e + f_P, & \text{if } |k\rangle \in P_{3/2}. \end{cases}$$

Equation (7) utilizes a characteristic stretched state transition matrix element, $\mu \stackrel{\text{def}}{=} \langle P_{3/2},\ F = 3,\ m_F = 3|d_+|S_{1/2},\ F = 2,\ m_F = 2\rangle$ to properly scale a given reduced matrix element, $\langle f|d\cdot\varepsilon|i\rangle/\mu$, with d_+, the

right circular component of the dipole operator. The Wigner–Eckart theorem [38] and Breit–Rabi formula [39] can then be used to express an arbitrary transition matrix element $\langle f|d\cdot\varepsilon|i\rangle$ between two hyperfine levels $|i\rangle$ and $|f\rangle$.

To accurately model the system dynamics, it is necessary to account for the undesired off-resonant coupling of a given sideband transition described by equation (6) to an additional mode ν_2, given by

$$H^{\nu_2}_{\mathrm{blue},i,f} = \frac{\eta_{\nu_2}}{\eta_{\nu_1}}\Omega^{2p}_{\mathrm{blue},i,f}(|f\rangle\langle i|\otimes\mathbb{1}_{\mathrm{qb2}}\otimes\mathbb{1}_{\nu_1}\otimes c^{+} + \mathbb{1}_{\mathrm{qb1}}\otimes|f\rangle\langle i|\otimes\mathbb{1}_{\nu_1}\otimes c^{+})\times \mathrm{e}^{-\mathrm{i}(\delta-\Delta_{\mathrm{blue},i,f})t} + \mathrm{h.c.}, \tag{8}$$

in the case of a blue sideband transition. In equation (8), δ is the detuning between the utilized mode ν_1 and ν_2, which couples off-resonantly. In the case of a red sideband transition, the off-resonant coupling takes the form of equation (8) under interchange of the annihilation and creation operators of the harmonic oscillator describing the ν_2 motional mode, c and c^{+}, and replacement of $\Delta_{\mathrm{blue},i,f}$ by $\Delta_{\mathrm{red},i,f}$, respectively.

2.4. Lindblad operators

Incoherent processes taking place alongside the driven transitions appear in the dissipative part $\mathcal{L}_{\mathcal{D}}$ in equation (1), which is comprised of individual contributions modeled by the Lindblad (jump) operators L_k in equation (2). An effective operator formalism [40] allows to adiabatically eliminate the hyperfine excited state addressed by the repump laser. It leads to Lindblad operators of the form [41]

$$L^{(1)}_{\mathrm{rep},i,f} = \sqrt{\gamma^{\mathrm{eff}}_{if}}|f\rangle\langle i|\otimes\mathbb{1}_{\mathrm{qb2}}\otimes\mathbb{1}_{\nu_1}\otimes\mathbb{1}_{\nu_2}, \tag{9}$$

$$L^{(2)}_{\mathrm{rep},i,f} = \sqrt{\gamma^{\mathrm{eff}}_{if}}\mathbb{1}_{\mathrm{qb1}}\otimes|f\rangle\langle i|\otimes\mathbb{1}_{\nu_1}\otimes\mathbb{1}_{\nu_2}, \tag{10}$$

with effective rates

$$\gamma^{\mathrm{eff}}_{if} = \gamma_{ef}\frac{4\Omega^2_{\mathrm{car},i,e}}{\gamma^2}, \tag{11}$$

where $|e\rangle$ is the intermediate, rapidly decaying, electronically excited state, $\Omega_{\mathrm{car},i,e}$ the repump Rabi frequency, γ_{ef} the decay rate from $|e\rangle$ into the hyperfine ground state $|f\rangle$ and $\gamma=\sum_{f'}\gamma_{ef'}$ the total decay rate out of $|e\rangle$ into a subspace of hyperfine ground states.

Similarly to equations (9), (10), leaking between ground-state hyperfine levels due to stimulated Raman sideband transition acts on both beryllium ions according to

$$L^{(1)}_{\mathrm{sid},i,f} = \sqrt{\Gamma_{if}}|f\rangle\langle i|\otimes\mathbb{1}_{\mathrm{qb2}}\otimes\mathbb{1}_{\nu_1}\otimes\mathbb{1}_{\nu_2}, \tag{12}$$

$$L^{(2)}_{\mathrm{sid},i,f} = \sqrt{\Gamma_{if}}\mathbb{1}_{\mathrm{qb1}}\otimes|f\rangle\langle i|\otimes\mathbb{1}_{\nu_1}\otimes\mathbb{1}_{\nu_2}. \tag{13}$$

The scattering rate Γ_{if} between an initial hyperfine ground state $|i\rangle$ and a final hyperfine ground state $|f\rangle$, due to a single laser beam is given by the Kramers–Heisenberg formula

$$\Gamma_{if} = \Gamma_{i\to f} = \frac{|E|^2\mu^2}{4}\gamma\left|\sum_k\frac{a^{(k)}_{if}}{\Delta_k}\right|^2, \tag{14}$$

where

$$a^{(k)}_{if} = a^{(k)}_{i\to f} = \sum_{q\in\{+,0,-\}}\frac{\langle f|d_q|k\rangle}{\mu}\frac{\langle k|d\cdot\varepsilon|i\rangle}{\mu} \tag{15}$$

is the two-photon transition amplitude between $|i\rangle$ and $|f\rangle$. As in equation (7), k runs over all states $|k\rangle$ belonging to the $^9\mathrm{Be}^{+}$ ion $P_{1/2}$ and $P_{3/2}$ manifolds. Again, it sufficies to approximate the Δ_k of $k\in P_{1/2}$, $P_{3/2}$ as Δ_e and Δ_e+f_P, respectively. Rayleigh scattering is modeled by a Pauli σ_z matrix between pairs of levels. Acting at the rate

$$\phi_{if} = \frac{|E|^2\mu^2}{4}\gamma\left|\sum_k\left(\frac{a^{(k)}_{ii}}{\Delta_k}-\frac{a^{(k)}_{ff}}{\Delta_k}\right)\right|^2, \tag{16}$$

Rayleigh scattering is only of concern between the $|\downarrow\rangle$ and $|\uparrow\rangle$ levels and in most cases negligibly small.

Sympathetic cooling is achieved by using stimulated Raman laser cooling and can be made to affect either or both of the considered motional modes according to

$$L_{\mathrm{cool},\nu_1} = \sqrt{\kappa_{c,\nu_1}}\mathbb{1}_{\mathrm{qb1}}\otimes\mathbb{1}_{\mathrm{qb2}}\otimes b\otimes\mathbb{1}_{\nu_2}, \tag{17}$$

$$L_{\text{cool},\nu_2} = \sqrt{\kappa_{c,\nu_2}}\mathbb{1}_{\text{qb1}} \otimes \mathbb{1}_{\text{qb2}} \otimes \mathbb{1}_{\nu_1} \otimes c, \tag{18}$$

where the cooling rates κ_{c,ν_1} and κ_{c,ν_2} are governed by the field strengths of the repump and stimulated Raman lasers acting on the magnesium ions.

Heating acts on all motional modes. It is caused by spontaneous emission occuring during the magnesium sideband Raman transitions, as well as photon recoil from spontaneous emission and also the anomalous heating of the ion trap. The total heating can be modeled by

$$L_{\text{heat},\nu_1} = \sqrt{\kappa_{h,\nu_1}}\mathbb{1}_{\text{qb1}} \otimes \mathbb{1}_{\text{qb2}} \otimes b^\dagger \otimes \mathbb{1}_{\nu_2}, \tag{19}$$

$$L_{\text{heat},\nu_2} = \sqrt{\kappa_{h,\nu_2}}\mathbb{1}_{\text{qb1}} \otimes \mathbb{1}_{\text{qb2}} \otimes \mathbb{1}_{\nu_1} \otimes c^\dagger, \tag{20}$$

for a set of given heating rates κ_{h,ν_1} and κ_{h,ν_2}.

3. Optimizing the original scheme

The goal of optimization is to maximize the population in the target state $|S_{\downarrow\uparrow}\rangle$. To this end, the final time T is defined as the time at which the peak population in the target state is reached and all driving fields can be turned off. The target state population at final time is defined as the fidelity F and correspondingly the error as $\epsilon \stackrel{\text{def}}{=} 1 - F$. The peak population at the final time is an appropriate quantity to observe, since the stability of the ionic hyperfine ground states causes the system to remain in its entangled state for a long time after all driving fields have been turned off.

In the following, the system degrees of freedom available for control are introduced and categorized into two collections in preparation for the optimization scheme discussed below. In contrast to a straightforward parameter optimization of all degrees of freedom, the specialized optimization scheme presented here is less susceptible to running into local minima and demonstrates reliable and fast convergence.

3.1. Optimization parameters

As previously discussed, the limitations of the original scheme [32] are fundamentally linked to the physical process of the stimulated Raman sideband transition. The two-photon Rabi frequency $\Omega^{2p}_{\text{blue},\downarrow,\uparrow}$ associated with this transition should be made as large as possible to drive the system towards the desired target state whilst ensuring that the unfavorable transition between $|S_{\downarrow\uparrow}\rangle$ and $|S_{a\downarrow}\rangle$ is suppressed. Consequently, the carrier transition Rabi rate $\Omega_{\text{car},a,\uparrow}$ and in turn the repump transition Rabi rate governing the effective decay out of $|a\rangle$ are limited, bottlenecking the flow of population into the target state.

Equations (7), (14), (15) show that merely increasing the field strengths of the sideband lasers has the adverse side effect of also increasing the chance of photon scattering and therefore the rates of leaking between hyperfine ground states. As such, a safe way of increasing the field strength of the sideband lasers is to compensate by increasing the detuning Δ_e from the excited state manifold, since the two-photon Rabi frequency scales inversely with the detuning whilst the scattering rates between hyperfine states scale with the square of the inverse detuning. The field strengths required to significantly increase the two-photon Rabi frequency whilst minimizing the associated scattering rates are, however, beyond current experimental capabilities [42]. A third option is given by the polarization of the two stimulated Raman sideband laser beams ε_r and ε_b, which have a great impact on both $\Omega^{2p}_{\text{blue},\downarrow,\uparrow}$ and also $\{\Gamma_{if}\}$.

The tunable parameters E_r and E_b, ε_r and ε_b and Δ_e, appearing in equations (7), (14), (15) constitute a first set of parameters defined as

$$\mathcal{P}_{\text{inner}} \stackrel{\text{def}}{=} \{E_r, E_b, \varepsilon_r, \varepsilon_b, \Delta_e\}. \tag{21}$$

These are directly associated with the stimulated Raman sideband transition. The two-photon Rabi frequency $\Omega^{2p}_{\text{blue},\downarrow,\uparrow}$ scales with the product of field strengths E_rE_b, whilst the scattering rates due to each laser beam scale with $|E_{r/b}|^2$, the magnitude of the field strength squared. The polarization is split into its three spherical components, $\varepsilon = (\varepsilon_-, \varepsilon_0, \varepsilon_+)$ where $\varepsilon_i \in [-1, 1]$, $\forall\, i \in \{-,0,+\}$ and with

$$|\varepsilon_-|^2 + |\varepsilon_0|^2 + |\varepsilon_+|^2 = 1. \tag{22}$$

Due to the normalization of the spherical components, each polarization possesses two degrees of freedom which can be represented as the azimuthal and polar angles on the unit sphere.

A given configuration of $\mathcal{P}_{\text{inner}}$ fully determines the resulting two-photon Rabi frequency $\Omega^{2p}_{\text{blue},\downarrow,\uparrow}$ and all leakage rates Γ_{if} between hyperfine states. These parameters are deliberately regarded separately from a second set of parameters

$$\mathcal{P}_{\text{outer}} \stackrel{\text{def}}{=} \{\Omega_{\text{car},a,\uparrow}, \Omega_{\text{car},a,e}, \Delta_{\text{car},a,\uparrow}, \Delta_{\text{blue},\downarrow,\uparrow}, a\}, \tag{23}$$

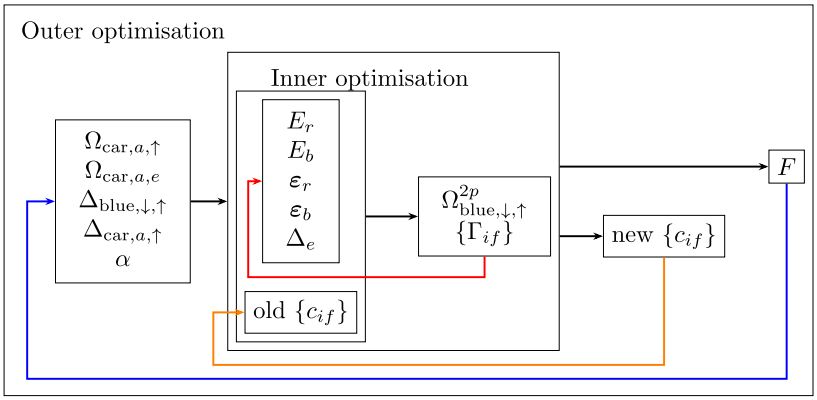

Figure 3. Schematic overview of the two-step parameter optimization algorithm for the two sets of parameters, $\mathcal{P}_{\mathrm{inner}}$ and $\mathcal{P}_{\mathrm{outer}}$. The inner optimization (red loop) depends on $\mathcal{P}_{\mathrm{inner}}$ and a set of weights $\{c_{if}\}$. After the inner optimization, the old set of weights can be updated (orange loop) and the fidelity F of the dynamics is optimized in an outer (blue) loop.

consisting of the carrier Rabi frequencies and detunings for both ground state transitions and a balance parameter a, which shall become important during the optimization. The carrier Rabi frequencies are directly determined by the applied field strengths and can be tuned over broad ranges. The detunings $\Delta_{\mathrm{car},a,\uparrow}$ and $\Delta_{\mathrm{blue},\downarrow,\uparrow}$ should be kept small to prevent off-resonant coupling to additional motional modes.

3.2. Optimization algorithm

Our optimization algorithm, schematically depicted in figure 3, takes the approach of optimizing the sets introduced above in a two-step process. Conceptually, the inner optimization over the first set of parameters $\mathcal{P}_{\mathrm{inner}}$ incorporates the dynamics indirectly and is encapsulated by an outer optimization over the second set of parameters $\mathcal{P}_{\mathrm{outer}}$, maximizing the actual fidelity F. This strategy is motivated by the fact that determining $\Omega^{2p}_{\mathrm{blue},\downarrow,\uparrow} = \Omega^{2p}_{\mathrm{blue},\downarrow,\uparrow}(E_r, E_b, \varepsilon_r, \varepsilon_b, \Delta_e)$ and $\{\Gamma_{if} = \Gamma_{if}(E_r, E_b, \varepsilon_r, \varepsilon_b, \Delta_e)\}$ does not require explicit knowledge of the dynamics and is therefore computationally inexpensive.

The target functional of the inner step of the optimization depends on the field strengths E_r and E_b, polarizations ε_r and ε_b and excited state detuning Δ_e and is defined as

$$J_{\mathrm{inner}}[E_r, E_b, \varepsilon_r, \varepsilon_b, \Delta_e] = \sum_{if} c_{if}\Gamma_{if} - \alpha\Omega^{2p}_{\mathrm{sid}}. \tag{24}$$

Here, α is a balance parameter which weights up the relative importance of maximizing $\Omega^{2p}_{\mathrm{blue},\downarrow,\uparrow}$ versus minimizing the sum $\sum_{if} c_{if}\Gamma_{if}$, for a given set of weights $\{c_{if}\}$. If the set of weights $\{c_{if}\}$ and a are fixed, the inner optimization can calculate $\Omega^{2p}_{\mathrm{blue},\downarrow,\uparrow}$ and $\{\Gamma_{if}\}$ in terms of $\mathcal{P}_{\mathrm{inner}}$, which are passed back to the outer part of the optimization, once J_{inner} is minimal.

The optimization of the set of parameters $\mathcal{P}_{\mathrm{inner}}$ requires a measurement of the effect a change in each scattering rate Γ_{if} has on F, the overall fidelity of the dynamics. This runs contrary to the usual practice of minimizing the total scattering rate $\sum_{if}\Gamma_{if}$ between all pairs of ground state hyperfine levels. Individually weighting each Γ_{if} comes as a consequence of the observation that the leaking between each pair of hyperfine ground states affects the reached fidelity differently. Most notably, transitions leading out of the steady state $|S_{\downarrow\uparrow}\rangle$ and transitions leading out of the hyperfine subspace $\{a, \downarrow,\uparrow\}$ into the neighboring states $\{o, t\}$ have the largest negative effect on the fidelity. Taking into account each individual leaking rate therefore offers the possibility of strongly suppressing certain detrimental Γ_{if} by carefully tuning the polarization. We encode the degree to which a certain Γ_{if} affects the fidelity by running several simulations where each individual rate Γ_{if} is artificially boosted by a factor of 10, whilst keeping all other rates fixed, resulting in a set of fidelities $\{F_{if}\}$. Observing the difference $F - F_{if}$, between boosted and unaltered dynamics leads to a set of weights, $\{c_{if} \stackrel{\mathrm{def}}{=} 1000(F - F_{if})\}$.

Figure 4 shows two different sets of weights at the beginning of the optimization and after a few updates. As discussed in [32] the biggest scattering error is due to the qubit transition between $|\uparrow\rangle$ and $|\downarrow\rangle$. $\Gamma_{\uparrow\downarrow}$, Along with transitions leading out of the hyperfine subspace into the neighboring $|o\rangle$ and $|t\rangle$ levels, received the largest weights c_{if} for the duration of the optimization.

A given set of weights can be used to optimize $\mathcal{P}_{\mathrm{inner}}$, leading to the best possible $\Omega^{2p}_{\mathrm{blue},\downarrow,\uparrow}$ and $\{\Gamma_{if}\}$ with which to perform the dynamics.

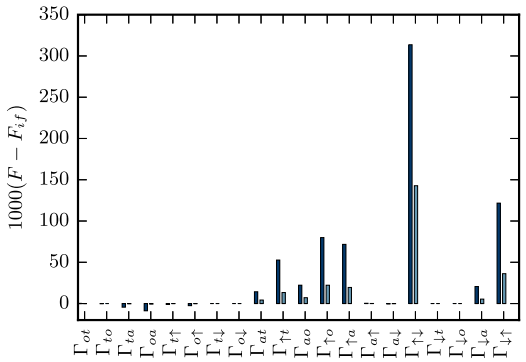

Figure 4. Change in fidelity $F - F_{if}$ between unaltered dynamics and dynamics resulting from artificially boosting a specific Γ_{if}. The dark blue set of weights generated in the first iteration is different from the pale blue set of weights generated after several updates.

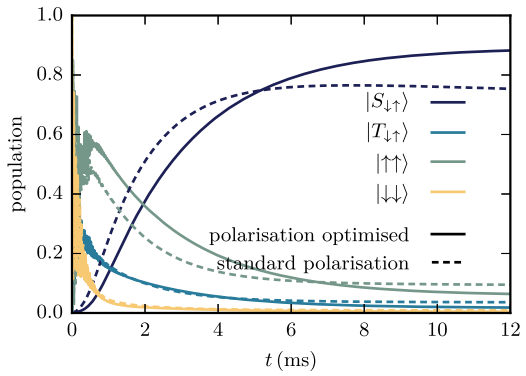

Figure 5. Time-dependent population in the states $|\downarrow\downarrow\rangle$, $|\uparrow\uparrow\rangle$, $|S_{\downarrow\uparrow}\rangle$ and $|T_{\downarrow\uparrow}\rangle$ after summing over all motional levels. The graph compares the dynamics when starting with all population in the $|\downarrow\downarrow\rangle$ state initially, before (dashed lines) and after (solid lines) the combined optimization, leading to fidelities of $F = 76\%$ and 88%, respectively.

The optimization of the second set of parameters, $\mathcal{P}_{\text{outer}}$, directly targets the fidelity F of the dynamics

$$J_{\text{outer}}[\Omega_{\text{car},a,\uparrow}, \Omega_{\text{car},a,e}, \Delta_{\text{blue},\downarrow,\uparrow}, \Delta_{\text{car},a,\uparrow}, \alpha] \stackrel{\text{def}}{=} 1 - F = \epsilon. \tag{25}$$

For each iteration of the outer optimization, the inner optimization over equation (24) leading to optimal $\Omega^{2p}_{\text{blue},\downarrow,\uparrow}$ and $\{\Gamma_{if}\}$ is performed using the set of weights $\{c_{if}\}$ generated during the previous iteration (for the first iteration $c_{if} = 1$, $\forall\, i, f$). After the inner optimization, a new set of weights $\{c_{if}\}$ is generated for the next iteration of the outer optimization, as illustrated in figure 3.

This two-step optimization is easily generalized for arbitrary combinations of transitions, including the possibility for multiple sideband transitions between differentground state hyperfine levels. Optimization of multiple sideband transitions follows the rule, that the jth sideband transition has its own set of polarizations $\varepsilon_r^{(j)}$ and $\varepsilon_b^{(j)}$, field strengths $E_r^{(j)}$ and $E_b^{(j)}$, balance parameter $\alpha^{(j)}$ and excited state detuning $\Delta_e^{(j)}$ but each contributes towards a set of total scattering rates $\{\Gamma_{if} = \sum_j \Gamma_{if}^{(j)}\}$. Furthermore, all transitions except for the repump transition have a detuning $\Delta_{\text{type},i,f}$ and all carrier transitions have a Rabi frequency $\Omega_{\text{car},i,f}$ to be optimized directly, along with the set of balance parameters $\{\alpha^{(j)}\}$, in the outer optimization.

3.3. Result of optimization

All parameter optimizations have been performed with the NLopt package [43] using the Subplex algorithm [44]. While other optimization methods could also be used in the outer and inner optimization loops, we have found these to converge well. Figure 5 compares the simulated dynamics of the system as described in [32] with the dynamics obtained after optimization. The peak fidelity is increased from $F = 76\%$ to $F = 88\%$. This is due to a modified steady state, in which the populations in $|T_{\downarrow\uparrow}\rangle$, $|\uparrow\uparrow\rangle$ and $|\downarrow\downarrow\rangle$ each are smaller than in the original scheme. Furthermore, through optimization of the Γ_{if}, a significant portion of the population can be prevented from escaping the ground state hyperfine subspace $\{a, \downarrow, \uparrow\}$, which causes the prominent crest in the $|S_{\downarrow\uparrow}\rangle$ population for the original scheme. The optimized result was compared to different realizations of randomly

Table 1. Optimized parameters when using the same transitions as in [32], leading to a fidelity of $F = 88\%$, compared to $F = 76\%$ in [32]. Both field strengths E_r and E_b are limited to the maximum values of 7520 V m^{-1}. $\Omega^{2p}_{\mathrm{blue},\downarrow,\uparrow}$ is determined by equation (7), $\Omega_{\mathrm{car},a,e}$ leads to γ_{if} in equations (9), (10).

Quantity	E_r	E_b	ε_r	ε_b	$\frac{\Omega_{\mathrm{car},a,\uparrow}}{2\pi}$	$\frac{\Omega^{2p}_{\mathrm{blue},\downarrow,\uparrow}}{2\pi}$	$\frac{\Omega_{\mathrm{car},a,e}}{2\pi}$	$\Delta_{\mathrm{car},a,\uparrow}$	$\Delta_{\mathrm{blue},\downarrow,\uparrow}$	Δ_e
Value	7520 V m^{-1}	7520 V m^{-1}	(0.162, 0.987, 0.000)	(−0.870, −0.286, −0.403)	316 Hz	7.65 kHz	179 kHz	−46 Hz	−44 Hz	662 GHz

chosen polarizations ε_r and ε_b, which leads to dramatically varying peak fidelities that can be as low as $F = 10\%$ but are only rarely in the vicinity of but never surpass the peak fidelity reached by optimization.

The optimized values of the various parameters are reported in table 1. After optimization, the two-photon sideband Rabi frequency $\Omega^{2p}_{\mathrm{blue},\downarrow,\uparrow}$ assumes a value of $2\pi \times 7.65$ kHz, which is very close to the rate $2\pi \times 7.81$ kHz reported in [32]. The increase in fidelity can therefore mainly be attributed to the adjustments made to the polarization ε_r, ε_b and increase in excited state manifold detuning Δ_e from 270 GHz to 662 GHz, which is feasible, see for example in [45]. In other words, the outcome of the inner optimization is a superior set of scattering rates $\{\Gamma_{if}\}$, with the parameters of the outer optimization adjusted to rebalance the system. Compared to [32], in which $\Omega_{\mathrm{car},a,\uparrow} = 495$ Hz, the carrier Rabi frequency between $|a\rangle$ and $|\uparrow\rangle$ drops to 316 Hz after optimization, thus further suppressing the unwanted $|S_{\downarrow\uparrow}\rangle \leftrightarrow |S_{a\downarrow}\rangle$ transition. As the optimal fidelity is approached, the detunings $\Delta_{\mathrm{car},a,\uparrow}$ and $\Delta_{\mathrm{blue},\downarrow,\uparrow}$ become negligibly small, indicating that for this particular entanglement scheme, the shift out of resonance due to the driven transitions is not much of a factor.

Nevertheless, the achievable fidelity is inherently limited in this entanglement scheme. As demonstrated by equations (7), (14), (15), even if the field strengths of the lasers utilized for the stimulated Raman sideband transition were unconstrained, a finite amount of leaking between hyperfine states would remain present. Limited field strengths of the sideband lasers necessitate a trade-off between the error due to leaking between hyperfine states and the errors due to population trapping in $|\uparrow\uparrow\rangle$ and the unfavorable transition between $|S_{\downarrow\uparrow}\rangle$ and $|S_{a\downarrow}\rangle$.

As such, the fidelity that can be reached with our optimized parameters falls short of the fidelity obtained by switching to the stepwise scheme presented in [32] which amounts to $F = 89.2\%$. The stepwise scheme negates the error caused by the unfavorable transition between $|S_{\downarrow\uparrow}\rangle$ and $|S_{a\uparrow}\rangle$ by temporally separating the ground state hyperfine transitions from the application of the repumper and also the sympathetic cooling. This strategy ensures that population lost out of $|S_{\downarrow\uparrow}\rangle$ into $|S_{a\uparrow}\rangle$ has nowhere to go and, if precisely timed, is returned to $|S_{\downarrow\uparrow}\rangle$ after a full Rabi cycle. Essentially, the stepwise scheme lifts the requirement of balancing the rates at which each transition can be driven, thereby overcoming the limitations associated with the time-continuous implementation. In the following we will show that a continuously operated scheme can outperform both variants for entanglement generation of [32] by exploiting a different combination of transitions.

4. Two-sideband scheme

Alternatively to the original scheme presented in (2.2), steady-state entanglement can be reached using other combinations of continuously driven carrier and sideband $^9Be^+$-hyperfine transitions. We consider here a scheme that features two sideband transitions: a blue sideband transition from $|\downarrow\rangle$ to $|\uparrow\rangle$, and a second, red sideband transition from $|\uparrow\rangle$ to $|a\rangle$. Note that we assume each sideband transition to be driven by its own pair of stimulated Raman laser beams. It would also be possible to drive the two sideband transitions using only three beams. This simply requires proper choice of the correct relative detunings. In addition, and as in the original scheme, a repump transition between $|a\rangle$ and $|e\rangle$ is driven. In order for all states in the hyperfine subspace to be connected to the target state $|S_{\downarrow\uparrow}\rangle$, a carrier transition between $|\downarrow\rangle$ and $|\uparrow\rangle$ is included as well. This choice is similar to the combination of transitions utilized for the entanglement of two $^{40}Ca^+$ ions in [20]. It offers numerous advantages over the original scheme as detailed below.

4.1. Entanglement mechanism and optimization parameters

Figure 6 illustrates the entanglement mechanism for this new combination of transitions. Crucially, the unfavorable transition between $|S_{\downarrow\uparrow}\rangle \otimes |0\rangle$ and $|S_{a\uparrow}\rangle \otimes |0\rangle$ due to the carrier connecting $|a\rangle$ and $|\uparrow\rangle$ in the original scheme has been eliminated. Instead, the red sideband transition from $|\uparrow\rangle$ to $|a\rangle$ leads from $|S_{\downarrow\uparrow}\rangle \otimes |n_{\nu_1}\rangle$ to $|S_{a\downarrow}\rangle \otimes |n_{\nu_1} - 1\rangle$ only when $n_{\nu_1} > 0$. Consequently, for this combination of transitions, in the absence of leakage between hyperfine states and heating, $|S_{\downarrow\uparrow}\rangle \otimes |n_{\nu_1} = 0\rangle$ alone is the steady state of the dynamics. In the presence of heating, population in $|S_{\downarrow\uparrow}\rangle \otimes |0\rangle$ can only escape due to an excitation of the utilized vibrational mode ν_1 followed by a sideband transition from $|S_{\downarrow\uparrow}\rangle \otimes |n_{\nu_1}\rangle$ to $|S_{a\downarrow}\rangle \otimes |n_{\nu_1} - 1\rangle$. Population in $|S_{a\downarrow}\rangle \otimes |n_{\nu_1} - 1\rangle$ can take multiple branching paths, all of which eventually lead back to $|S_{\downarrow\uparrow}\rangle$. As such, in contrast to the original scheme, which relies on sympathetic cooling, this particular combination of transitions inherently cools the utilized mode ν_1 of the system during entanglement generation.

Without the need for sympathetic cooling, the $^{24}Mg^+$ ions can be removed. This leads not only to a simplification of the experiment but also reduces the number of motional modes of the ionic crystal. It thus effectively eliminates the error due to off-resonant coupling to ν_2, given by equation (8) in the original scheme. As described in section 3, in the original scheme the carrier Rabi frequencies $\Omega_{\mathrm{car},a,\uparrow}$ and $\Omega_{\mathrm{car},a,e}$, which determine the rate of effective decay out of $|a\rangle$, are limited by the maximum attainable $\Omega^{2p}_{\mathrm{blue},\downarrow,\uparrow}$. In contrast, in the current scheme the carrier Rabi frequencies $\Omega_{\mathrm{car},\downarrow,\uparrow}$ and $\Omega_{\mathrm{car},a,e}$ can be increased significantly, without

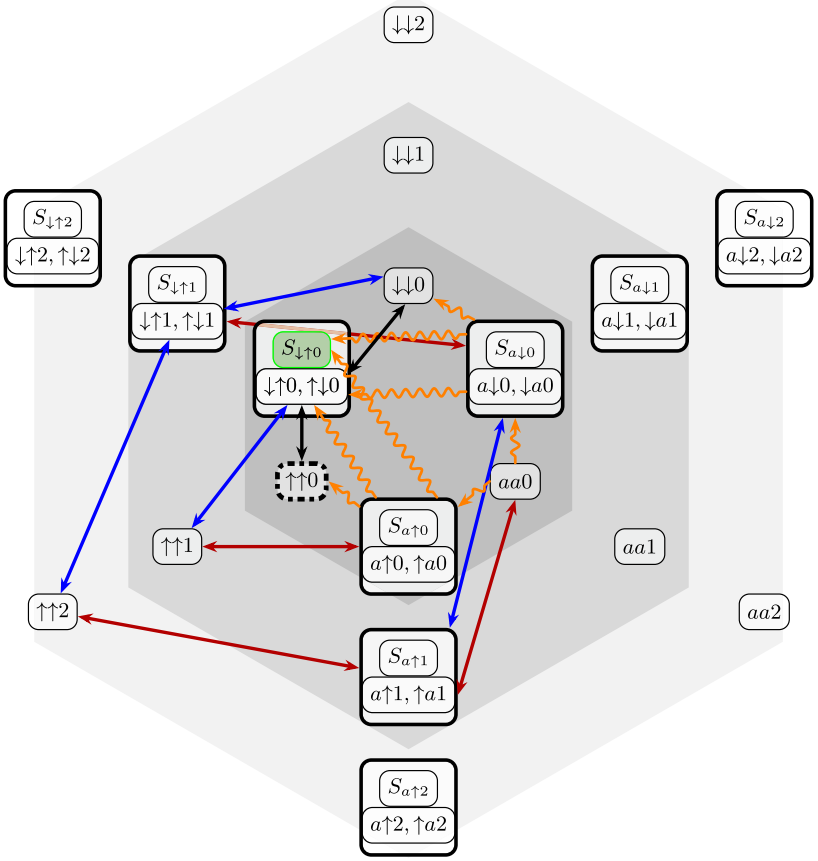

Figure 6. Graphical overview of transitions for the two-sideband transition scheme. As in the original scheme, only the most critical transitions for entanglement are shown and only states of the hyperfine subspace $\{a, \downarrow, \uparrow\}$ and the ν_1 motional mode are displayed. Carrier transitions between $|\downarrow\rangle$ and $|\uparrow\rangle$ at rate $\Omega_{\text{car},\downarrow,\uparrow}$ appear as black double-headed arrows. The blue $|\downarrow\rangle \rightarrow |\uparrow\rangle$ sideband transitions act at a rate of $\Omega^{2p}_{\text{blue},\downarrow,\uparrow}$ and appear as blue double headed arrows, whilst the red $|\uparrow\rangle \rightarrow |a\rangle$ sideband transitions acts at a rate $\Omega^{2p}_{\text{red},\uparrow,a}$ and appear as red double headed arrows. Effective decay out of $|a\rangle$ into the hyperfine subspace appears as orange snaking lines. Sympathetic cooling is no longer incorporated into the mechanism and heating of the motional mode and leaking between hyperfine states are not shown.

causing losses out of the target state and population trapping in $|\uparrow\uparrow\rangle$. By driving an additional sideband transition, the graph of states in figure 6 is more connected, permitting population to reach $|S_{|\downarrow\uparrow\rangle}\rangle$ by additional paths. Comparing the graphs shown in figures 2, 6, the combined effect of additional paths into the target state and the increase in $\Omega_{\text{car},a,e}$ which results in larger effective decay rates $\{\gamma_{a,f} \propto \Omega^2_{\text{car},a,e}\}$ should lead to much faster entanglement preparation.

Optimization of the field strengths and polarizations for the two-sideband scheme has been carried out according to the same principle as described in section 3, with the slight complication of having to address additional degrees of freedom. In the specific case of the two-sideband combination, the corresponding form of the target functional for the polarization optimization, equation (24), becomes

$$J_{\text{inner}}[E_b^{(1)}, E_r^{(1)}, \varepsilon_b^{(1)}, \varepsilon_r^{(1)}, \Delta_e^{(1)}, E_b^{(2)}, E_r^{(2)}, \varepsilon_b^{(2)}, \varepsilon_r^{(2)}, \Delta_e^{(2)}] = \sum_{if} c_{if}\Gamma_{if} - \alpha^{(1)}\Omega^{2p\ (1)}_{\text{blue},\downarrow,\uparrow} - \alpha^{(2)}\Omega^{2p\ (2)}_{\text{red},\uparrow,a}. \tag{26}$$

As in the original scheme and described in detail in section 3, optimization of the polarization can be accomplished without having to simulate the dynamics in each iteration. A single inner optimization step determines both $\Omega^{2p\ (1)}_{\text{blue},\downarrow,\uparrow} = \Omega^{2p\ (1)}_{\text{blue},\downarrow,\uparrow}(E_r^{(1)}, E_b^{(1)}, \varepsilon_r^{(1)}, \varepsilon_b^{(1)}, \Delta_e^{(1)})$ and $\Omega^{2p\ (2)}_{\text{red},\uparrow,a} = \Omega^{2p\ (2)}_{\text{red},\uparrow,a}(E_r^{(2)}, E_b^{(2)}, \varepsilon_r^{(2)}, \varepsilon_b^{(2)}, \Delta_e^{(2)})$, in addition to $\{\Gamma_{if} = \Gamma_{if}^{(1)}(E_r^{(1)}, E_b^{(1)}, \varepsilon_r^{(1)}, \varepsilon_b^{(1)}, \Delta_e^{(1)}) + \Gamma_{if}^{(2)}(E_r^{(2)}, E_b^{(2)}, \varepsilon_r^{(2)}, \varepsilon_b^{(2)}, \Delta_e^{(2)})\}$, the set of scattering rates due to each sideband transition. As in section 3, the outer optimization is performed directly on the fidelity F of the dynamics

$$J_{\text{outer}}[\Omega_{\text{car},\downarrow,\uparrow}, \Omega_{\text{car},a,e}, \Delta_{\text{car},\downarrow,\uparrow}, \Delta_{\text{blue},\downarrow,\uparrow}, \Delta_{\text{red},\uparrow,a}, \alpha^{(1)}, \alpha^{(2)}] \stackrel{\text{def}}{=} 1 - F = \epsilon. \tag{27}$$

The set $\mathcal{P}_{\text{outer}}$ now consists of the carrier Rabi frequencies $\Omega_{\text{car},\downarrow,\uparrow}, \Omega_{\text{car},a,e}$, the detunings $\Delta_{\text{car},\downarrow,\uparrow}, \Delta^{(1)}_{\text{blue},\downarrow,\uparrow}$ and $\Delta^{(2)}_{\text{red},\uparrow,a}$, of the microwave carrier, first and second sideband transitions, and the weights $\alpha^{(1)}$ and $\alpha^{(2)}$. Since the

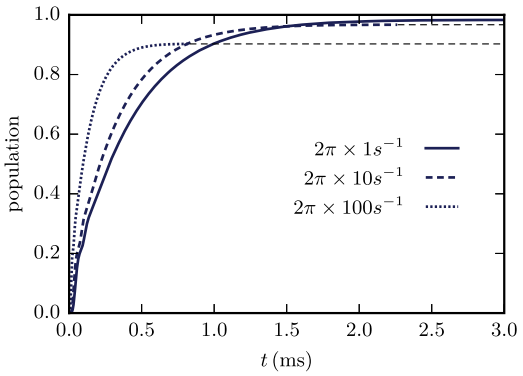

Figure 7. Population of the target state $|S_{\downarrow\uparrow}\rangle$ over time obtained with by optimization of the peak fidelity at final times T, for the two-sideband scheme with different assumed heating rates. The plot shows curves for the heating rates κ_{h} of $2\pi \times 1\ \mathrm{s}^{-1}$ (solid line) leading to a fidelity of $F = 98.3\%$, $2\pi \times 10\ \mathrm{s}^{-1}$ (dashed line) leading to $F = 96.7\%$ and $2\pi \times 100\ \mathrm{s}^{-1}$ (dotted line) leading to $F = 90.3\%$.

scheme now involves a second sideband combination, an additional weight is required to balance the maximization of its two-photon sideband Rabi frequency against the sideband photon scattering rates in equation (26). In order to make sure that both Rabi frequencies are maximized without one dominating the other, however, the left-hand side of equation (26) can be modified slightly, such that

$$\begin{aligned}\tilde{J}_{\mathrm{inner}}[&E_b^{(1)}, E_r^{(1)}, \varepsilon_b^{(1)}, \varepsilon_r^{(1)}, \Delta_e^{(1)}, E_b^{(2)}, E_r^{(2)}, \varepsilon_b^{(2)}, \varepsilon_r^{(2)}, \Delta_e^{(2)}] \\ &= \sum_{if} c_{if}\Gamma_{if} - \alpha(\Omega^{2p\ (1)}_{\mathrm{blue},\downarrow,\uparrow} + \Omega^{2p\ (2)}_{\mathrm{red},\uparrow,a}) + \beta|\Omega^{2p\ (1)}_{\mathrm{blue},\downarrow,\uparrow} - \Omega^{2p\ (2)}_{\mathrm{red},\uparrow,a}|,\end{aligned} \tag{28}$$

where α now balances the maximization of the sum of two-photon Rabi frequencies against the Γ_{if}, whilst β is a parameter controlling how strictly the two-photon sideband Rabi frequencies should be matched. For simplicity it is assumed that $E_r^{(1)} = E_r^{(2)}$ and $E_b^{(1)} = E_b^{(2)}$ and that each field strength is limited to the maximum value allowed during the optimization of the original scheme.

In the absence of sympathetic cooling, the primary source of heating, caused by spontaneous emission during the stimulated Raman sideband transition driven on the $^{24}Mg^{+}$ ions, is eliminated. The remaining sources of heating are photon recoil from the spontaneous emission out of $|e\rangle$ after repumping and electric field noise associated with the ion trap [32]. Since the heating rate influences the system dynamics and therefore the obtained fidelity, the result of the optimization depends on the specific heating rate assumed, which can vary, depending on the motional mode utilized for the sideband transition.

4.2. Influence of trap heating rates

Figure 7 compares the reached peak fidelity for different values of the heating rate κ_{h} of vibrational mode ν_1. For an assumed heating rate of $\kappa_{\mathrm{h}} = 2\pi \times 1\ \mathrm{s}^{-1}$, optimization leads to a peak fidelity of $F = 98.3\%$, whilst $\kappa_{\mathrm{h}} = 2\pi \times 10\ \mathrm{s}^{-1}$ is a more realistic heating rate for modern traps leading to a peak fidelity of $F = 96.7\%$. Finally, when $\kappa_{\mathrm{h}} = 2\pi \times 100\ \mathrm{s}^{-1}$, the peak fidelity is reduced to $F = 90.3\%$. For each considered heating rate, the parameters leading to optimal entanglement are listed in table 2. As the heating rate κ_{h} is increased, recovering population lost from the target state $|S_{\downarrow\uparrow}\rangle$ requires an increase in the Rabi frequencies of all driven transitions. For all reported heating rates, however, the ratios $\Omega_{\mathrm{car},\downarrow,\uparrow} \propto \Omega^{2p\ (1)}_{\mathrm{blue},\downarrow,\uparrow} \approx \Omega^{2p\ (2)}_{\mathrm{red},\uparrow,a} \propto \Omega^2_{\mathrm{car},a,e}$ remain approximately constant. Here, the repumper Rabi frequency $\Omega_{\mathrm{car},a,e}$ enters squared, since the effective decay rates in equation (11) are proportional to $\Omega^2_{\mathrm{car},a,e}$. This observation can be understood, since the target state should be reachable as directly as possible from any given state. Scaling all transition rates equally is necessary in order to prevent the flow of population from being bottlenecked throughout the entanglement generation. The optimized peak fidelities are again significantly higher than the average fidelity of $F \approx 0.4$ (or $F \approx 0.5$ with the fixed scaling of Rabi frequencies mentioned above) obtained from simulating the dynamics with random polarizations $\varepsilon_r^{(1)}$, $\varepsilon_b^{(1)}$, $\varepsilon_r^{(2)}$ and $\varepsilon_b^{(2)}$ of the sideband laser beams and assuming $\kappa_{\mathrm{h}} = 2\pi \times 1\ \mathrm{s}^{-1}$. For the two-sideband scheme it is much more difficult to randomly select a near-optimal polarization, due to the increased number of degrees of freedom, which also causes the peak fidelity to strongly vary depending on the polarization. Furthermore, an optimization to minimize the time taken to reach a target state population of $F = 85\%$ was performed for the heating rates $\kappa_{\mathrm{h}} \in \{2\pi \times 1\ \mathrm{s}^{-1}, 2\pi \times 10\ \mathrm{s}^{-1}, 2\pi \times 100\ \mathrm{s}^{-1}\}$, leading to a preparation time of $t \approx 0.3$ ms for all assumed heating rates.

For each increase in the heating rate, the optimization results in a different set of polarizations $\varepsilon_r^{(1)}$, $\varepsilon_b^{(1)}$, $\varepsilon_r^{(2)}$ and $\varepsilon_b^{(2)}$. As the heating rate is increased, the minimization of leakage rates $\{\Gamma_{if}\}$ becomes less important. A given

Table 2. Optimized parameters for the two-sideband scheme. As for the original scheme, each field strength is limited to a maximum value of 7520 V m^{-1}. $\Omega^{2p\ (1)}_{\text{blue},\downarrow,\uparrow}$ and $\Omega^{2p\ (2)}_{\text{red},\uparrow,a}$ are both determined by equation (7) with individual polarizations $\varepsilon_r^{(1)}$, $\varepsilon_b^{(1)}$, $\varepsilon_r^{(2)}$ and $\varepsilon_b^{(2)}$. Optimization of the two-sideband scheme leads to fidelities of $F = 98.3\%$, 96.7% and 90.3% for heating rates of $\kappa_{\text{h}} = 2\pi \times 1$ s^{-1}, $2\pi \times 10$ s^{-1} and $2\pi \times 100$ s^{-1}, respectively. The sideband detunings $\Delta_e^{(1)}$ and $\Delta_e^{(2)}$ are defined as in (2.3) with the same assumed fine structure splitting $f_p = 197.2$ GHz.

Parameter $\kappa_{\text{h}}=$	$2\pi \times 1$ s^{-1}	$2\pi \times 10$ s^{-1}	$2\pi \times 100$ s^{-1}
E_r	7520 V m^{-1}	7520 V m^{-1}	7520 V m^{-1}
E_b	7520 V m^{-1}	7520 V m^{-1}	7520 V m^{-1}
$\varepsilon_r^{(1)}$	(−0.752, −0.220, −0.621)	(−0.620, −0.500, −0.605)	(−0.741, −0.338, −0.581)
$\varepsilon_b^{(1)}$	(0.440, 0.759, 0.480)	(0.536, 0.644, 0.545)	(0.408, 0.802, 0.435)
$\varepsilon_r^{(2)}$	(−0.413, −0.204, −0.888)	(−0.453, −0.854, −0.257)	(−0.479, −0.824, −0.303)
$\varepsilon_b^{(2)}$	(−0.415, −0.883, −0.218)	(−0.451, −0.250, −0.857)	(0.493, 0.261, 0.830)
$\Omega_{\text{car},\downarrow,\uparrow}$	$2\pi \times 2.24$ kHz	$2\pi \times 2.91$ kHz	$2\pi \times 6.67$ kHz
$\Omega^{2p\ (1)}_{\text{blue},\downarrow,\uparrow}$	$2\pi \times 4.96$ kHz	$2\pi \times 6.47$ kHz	$2\pi \times 14.92$ kHz
$\Omega^{2p\ (2)}_{\text{red},\uparrow,a}$	$2\pi \times 4.96$ kHz	$2\pi \times 6.47$ kHz	$2\pi \times 14.92$ kHz
$\Omega_{\text{car},a,e}$	$2\pi \times 691$ kHz	$2\pi \times 802$ kHz	$2\pi \times 1233$ kHz
$\Delta_e^{(1)}$	624 GHz	245 GHz	318 GHz
$\Delta_e^{(2)}$	464 GHz	372 GHz	206 GHz

Γ_{if} is determined by the polarization of each stimulated Raman laser beam and scales with the squared magnitude of the field strength $|E|^2$ whilst scaling inversely with the squared detuning from the excited state Δ_e (equations (14), (15)) of the considered laser beam. Instead, the maximization of the two-photon stimulated Raman sideband transition rates $\Omega^{2p\ (1)}_{\text{blue},\downarrow,\uparrow}$ and $\Omega^{2p\ (2)}_{\text{red},\uparrow,a}$ (equation (7)) is prioritized. The two-photon stimulated Raman sideband transition Rabi frequencies depend on the polarizations ε_r and ε_b of both laser beams, the product of field strengths E_rE_b and the detuning of both stimulated Raman laser beams from the excited state Δ_e. Larger sideband two-photon Rabi frequencies ensure that population can flow back into $|S_{\downarrow\uparrow}\rangle \otimes |0\rangle$ much faster than the heating can allow it to escape.

Increasing all of the transition rates has the side effect of speeding up the entanglement but limits the attainable fidelity, with an increased error due to population leaking outside of the hyperfine subspace $\{a, \downarrow,\uparrow\}$. The behavior of the $\Delta_e^{(1)}$ and $\Delta_e^{(2)}$ is non-monotonic and appears to be strongly dependent on the particular polarization profile. As in the original scheme, each of the $\Delta_{\text{car},\downarrow,\uparrow}$, $\Delta_{\text{blue},\downarrow,\uparrow}$ and $\Delta_{\text{red},\uparrow,a}$ becomes smaller as the optimal fidelity is reached.

The error due to heating can only be reduced by increasing the flow of population into the target state $|S_{\downarrow\uparrow}\rangle \otimes |0\rangle$, since there is no straightforward way to compensate for heating. This comes at the cost of increasing $\sum_{if} c_{if}\Gamma_{if}$ and thus the error due to leakage between the hyperfine states, as explained above. Assuming optimal polarization and balancing of the driven rates, the only way to reduce one error without compounding the other error is by increasing the maximum field strengths $E_r^{(1)}$, $E_b^{(1)}$, $E_r^{(2)}$ and $E_b^{(2)}$. This explains why the field strengths take their maximal allowed value in table 2.

4.3. Comparison to the original scheme

The two-sideband scheme represents a promising alternative to the original scheme even with optimized parameters, as discussed in section 3. In terms of fidelity, the two-sideband scheme outperforms the original one, regardless of the assumed heating rate κ_{h}. Even in the worst case considered, with $\kappa_{\text{h}} = 2\pi \times 100$ s^{-1}, the resulting error is under 10% after optimization. In comparison, the previously best fidelity, reached by the stepwise scheme in [32], corresponds to an error of about 11%. The corresponding errors for the original scheme in section 3 are slightly larger for the polarization optimized case and two and a half times as large for the non-optimized case. In terms of speed, the two-sideband scheme outperforms the original scheme. Given traps with sufficiently small heating rates, entangling speed can be sacrificed in order to maximize fidelity. The lowest regarded heating rate $\kappa_{\text{h}} = 2\pi \times 1$ s^{-1}, can be optimized over 3 ms, attaining a fidelity of $F = 98.3\%$, or optimized over 6 ms, in order to increase the fidelity to $F = 98.7\%$. In contrast, the original scheme peaks after approximately 6 ms but at the much lower fidelity $F = 76\%$.

To summarize, when considering the experimental modifications necessary to go from the protocol in [32] to the two-sideband scheme, the overall complexity is reduced. Instead of a four ion setup consisting of two ^{9}Be$^+$ and two ^{24}Mg$^+$ ions, with their respective sympathetic cooling laser beams, now only the two ^{9}Be$^+$ to be entangled need to be trapped without sympathetic cooling laser beams. Given sufficient power, the four laser beams required for both of the stimulated Raman sideband transitions can all be derived from the same 313 nm laser and frequency shifted using acousto-optic modulators. The only further complication is the ability to independently manipulate the polarization of each individual stimulated Raman sideband transition laser beam.

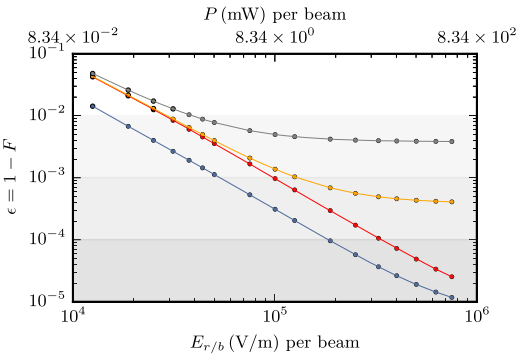

Figure 8. Bell state error $\epsilon = 1 - F$ as a function of the sideband laser beam strengths $E_{r/b}$ allowed during optimization. The red (orange and gray) points correspond to an ion trap with $\kappa_{\rm h} = 0$ ($\kappa_{\rm h} = 2\pi \times 1$ s^{-1} and $\kappa_{\rm h} = 2\pi \times 10$ s^{-1}, respectively). The blue points correspond to a three-beam configuration and $\kappa_{\rm h} = 0$. For all points, the detuning and carrier transition field strengths are chosen such that the fidelity peaks after an entangling duration of 1 ms. For zero heating, attaining a maximal error of $\epsilon < 0.001$ requires field strengths of 100 kV m^{-1}, or a combined power of 4×8.3 mW going into a 20 μm beam waist, whereas $\epsilon < 0.0001$ is reached when the optimization allows for amplitudes up to 325 kV m^{-1}, or a corresponding power of 4×89 mW.

One may wonder of course how sensitive the Bell state fidelity is with respect to small deviations from the optimized polarizations. We have found fluctuations in the polarization components of up to 5% to only have a neglible effect on the entanglement error, whilst fluctuations above 10% will noticeably reduce the fidelity.

4.4. Fundamental performance bound

Given the superior performance of the two-sideband scheme compared to the original protocol [32], one may wonder whether there are ultimate limits to the fidelity of a Bell state realized in this way. There are two main sources of error that limit the fidelities in this dissipative state preparation scheme—anomalous heating and spontaneous emission. As discussed above, the obtainable fidelity is determined by a trade-off between utilizing fast enough sideband transitions in order to beat trap heating, and minimization of the spontaneous emission rates associated with the sideband transitions. While anomalous heating can in principle be made arbitrarily small by improving the ion trap, undesired spontaneous emission is an inherent and unavoidable loss mechanism accompanying the desired spontaneous emission at the core of the dissipative state preparation. In order to explore the fundamental performance bound posed by spontaneous emission, we assume a realistic trap with $\kappa_{\rm h} = 2\pi \times 10$ s^{-1}, a close to perfect trap, with $\kappa_{\rm h} = 2\pi \times 1$ s^{-1} or no heating at all ($\kappa_{\rm h} = 0$ s^{-1}), and investigate how much laser power is needed to achieve a certain fidelity, or error.

In the absence of all heating, the optimization will favor slow sideband transitions that are detuned far below the $P_{1/2}$ and $P_{3/2}$ levels with laser beams polarized such that there is minimal spontaneous emission. Identifying the conditions under which it is possible to reach Bell state fidelities of $F = 99.9\%$ or even $F = 99.99\%$ allows us to benchmark the performance of the current dissipative scheme. For comparison, [42] examines the dependence of fidelity on laser power for gate-based entanglement creation for various ion species. Of all observed ion species, the gate error of ^{9}Be$^+$ entanglement was lowest for a given power P, related to the laser field strength E by

$$P = \frac{\pi}{4} E^2 w_0^2 c \epsilon_0, \tag{29}$$

where w_0 is the laser beam waist, c the speed of light and ϵ_0 the vacuum permittivity [42]. We assume here an (idealized) beam waist of $w_0 = 20$ μm, to directly compare to [42].

During optimization, the highest regarded threshold, $F = 99.99\%$ was reached after 0.33 ms using field strengths of $E_{r/b} \approx 752$ kV m^{-1} per beam and detunings up to 25 THz. For the sake of comparison with [42], and for the case of negligible heating, the timescale in the master equation (1) can be changed, $t \to \tau = \frac{t}{\chi}$. In order to match the same entangling speed and duration of 10 μs as reported in [42], we require 4.4 MV/m per beam, corresponding to a total power of 4×16 W at the same detuning. For this very fast entanglement, the negative effects of heating are limited, leading to errors of $\epsilon = 6.5 \times 10^{-5}$, $\epsilon = 1.0 \times 10^{-4}$ and $\epsilon = 4.47 \times 10^{-4}$ for heating rates of $\kappa_h \in \{2\pi \times 1$ s^{-1}, $2\pi \times 10$ s^{-1}, $2\pi \times 100$ s$^{-1}\}$, respectively.

If we fix the available field strength to the value $E_{r/b} \approx 200$ kV, corresponding to a total power of 4×36 mW, as reported in [42], the target fidelity is reached after 4.6 ms. Again, despite the much lower field strengths, the detuning remains unchanged. It should be noted here, that an entangling duration of 4.6 ms is still faster than that of the original entanglement scheme [32]. At this lower extreme in field strengths, the effects of

heating are more noticeable, since heating is allowed to act for almost 500 times longer relative to the 10 μs case.

Figure 8 shows the Bell state, i.e. entanglement error, obtained when rescaling the duration to 1 ms, for different field strengths $E_{r/b}$ and heating rates (shown in red, orange, and gray, respectively). A fidelity of $F = 99\%$ is reached for all regarded heating rates, requiring field strengths between $E_{r/b} = 31$ kV m^{-1} ($\kappa_{\mathrm{h}} = 2\pi \times 0$ s^{-1}) and $E_{r/b} = 38$ kV m^{-1} ($\kappa_{\mathrm{h}} = 2\pi \times 10$ s^{-1}). The next threshold, $F = 99.9\%$, is only crossed for $\kappa_{\mathrm{h}} = 0$ and $\kappa_{\mathrm{h}} = 2\pi \times 1$ s^{-1} at field strengths of $E_{r/b} = 100$ kV m^{-1} and $E_{r/b} = 125$ kV m^{-1}, corresponding to total powers of $P \approx 4 \times 8.3$ mW and $P \approx 4 \times 13$ mW, respectively. Obtaining this fidelity requires detunings on the order of 6 THz. The highest threshold, $F = 99.99\%$, is reached for $\kappa_{\mathrm{h}} = 2\pi \times 0$ s^{-1} whilst requiring field strengths of the order of $E_{r/b} \approx 325$ kV m^{-1} corresponding to a total power of 4×89 mW. This is about two and a half times more power than for the gate based approach in [42]. For neglible heating, the required field strength per beam can be reduced by using three instead of four beams to drive the two sideband transitions (blue curve in figure 8). This finding illustrates that parameter optimization is prone to trapping in local optima, in particular for a larger number of optimization parameters [46]. We attribute the improvement to the fact that omission of one beam reduces the inadvertent scattering. More specifically, the extra constraint on the beam detunings appears to aid the optimization algorithm in finding a configuration for which the contribution of each beam towards the scattering error is distributed in a more favorable way than in the four beam setup.

5. Conclusions

We have addressed the problem of additional noise sources that limit fidelity and speed of dissipative entanglement generation. Combining quantum optimal control theory [2] with the effective operator approach [41], we have shown how to improve both fidelity and speed for the example of entangling two hyperfine qubits in a chain of trapped ions [32]. The detrimental noise source in this case is undesired spontaneous decay brought about by the sideband laser beams that are necessary for coupling the qubits [32]. This decay leads to the irrevocable loss of population from the hyperfine subspace of interest. Whilst the undesired spontaneous decay cannot be eliminated entirely, an optimal choice of the experimental parameters increases the fidelity from 76% to 85%, with minimal changes to the setup. Key to the improvement is optimization of the sideband laser beam polarizations which enter the decay rates of each individual hyperfine level. Due to their interdependence, the various parameters of the experiment need to be retuned when changing the polarization. The two-stage optimization process that we have developed here can easily resolve this issue, demonstrating the power of numerical quantum control.

Further limitations to fidelity and speed can be identified graphically, by visualizing the connections between states due to the various field-driven transitions. This allows to qualitatively trace the flow of population and shows that, depending on the relative transition rates, population can get trapped in states other than the target state or be transferred out of the target state by an unfavorable transition. The latter in particular implies that the target state does not fully coincide with the steady state of the evolution. In order to overcome this limitation, we suggest to adapt the entanglement scheme presented in [20] to using two sideband transitions. Of course, adding a second sideband makes the suppression of the error due to detrimental spontaneous emission even more important. Our optimization method had no difficulty to cope with this task, despite the increase in the number of tunable parameters.

Analysis aided by the graph of connected states for the two-sideband scenario reveals that the limitations of the original scheme of [32] can indeed be overcome, whilst providing additional advantageous properties such as higher entanglement speed and inherent cooling. This offers the possibility of reducing the complexity of the experiment by removing the need for sympathetic cooling and all sources of error that come with it. The entangled, or, Bell state fidelity that we predict for the two-sideband scenario strongly depends on the heating rate. It can be as high as 98% under conditions similar to those of [32], in particular in terms of the available laser field strengths. The maximum attainable fidelity is primarily limited by the heating rate of the motional mode that is used to couple the qubits. It dictates the timescale at which the sideband transitions must take place. Weaker sideband transition rates in turn enable better suppression of spontaneous emission errors. Whilst a fidelity of 98% represents an order of magnitude improvement over the originally obtained fidelity, execution of most quantum protocols requires fidelities in excess of 99%. These could be achieved through experimental refinements, such as ion traps with weaker anomalous heating, more powerful sideband lasers [42], or use of optical instead of hyperfine qubits [36, 37].

Provided that heating rates can be made negligible, for instance by implementing the two-sideband scheme on the stretch rather than the center of mass mode of the two ions, one may wonder whether spontaneous emission ultimately limits the performance of dissipative Bell state preparation. Spontaneous emission can be reduced by using larger detunings which in turn requires more laser power or longer durations. Compared to

gate-based entanglement preparation [42], we find, for the same laser power of 4 × 36 mW into 20 μm beam waist as in [42], the entangling duration to realize a Bell state fidelity of 99.99% to be increased from 10 μs to 4.6 ms in an ideal trap. The advantages of the dissipative approach, in particular its inherent robustness against noise, might easily outweigh this time requirement, making dissipative entanglement production a viable resource for quantum information protocols. Consider, for example, carrying out primitives such as gate teleportation. This could be driven by an entanglement machine that produces 200 pairs/s in serial mode (per node) or output one pair per 10 μs when run with 250 nodes in parallel. A further speed up is possible by using more laser power.

Our study provides a first example for how to use quantum optimal control theory to push driven-dissipative protocols to their ultimate performance limit, despite imperfections in a practical setting. Performance limits include, in addition to maximal fidelity, also the highest speed. Here, we have obtained a speed up of about a factor of four compared to [32]. Speed is of particular concern when scaling up entanglement generation since some undesired decoherence rates are known to scale with system size [47]. Deriving the fastest possible protocol is therefore key if dissipative generation of many-body entanglement [23] is to succeed. As we have shown, optimal control theory is a tool ideally suited to tackle this task, and targeting a multipartite entangled state is a natural next step.

The optimal control theory framework for dissipative entanglement generation that we have introduced here is not limited to the specific example of trapped ions. In fact, our technique is applicable to generic multi-level quantum systems in the presence of dissipation for which the time evolution can be obtained within reasonable computation time[6]. This includes also systems with multiple steady states [48, 49] which would be interesting for e.g. quantum error correction, or systems with non-Markovian dynamics such as solid state devices [50]. In the latter case, the generalization requires the combination of the present optimization approach with one of the methods for obtaining non-Markovian dynamics [51], such as partitioning the environment into strongly and weakly coupled parts [52]. Non-Markovianity has been shown to assist entanglement generation in coupled dimers subject to dephasing noise [53]. Our approach would allow to investigate, for more complex systems and other types of dissipation, whether non-Markovianity is beneficial or detrimental to the speed and overall success of entanglement generation.

Acknowledgments

We thank Dave Wineland for discussions and Yong Wan and Stephen Erickson for helpful suggestions on the manuscript. Financial support from the Deutsche Forschungsgemeinschaft (Grant No. KO 2301/11-1) is gratefully acknowledged. Florentin Reiter acknowledges support by a Feodor-Lynen fellowship from the Humboldt Foundation.

ORCID iDs

Christiane P Koch https://orcid.org/0000-0001-6285-5766

References

[1] Breuer H-P and Petruccione F 2002 *The Theory of Open Quantum Systems* (Oxford: Oxford University Press)
[2] Glaser S J *et al* 2015 *Eur. Phys. J.* D **69** 279
[3] Caneva T, Murphy M, Calarco T, Fazio R, Montangero S, Giovannetti V and Santoro G E 2009 *Phys. Rev. Lett.* **103** 240501
[4] Goerz M H, Calarco T and Koch C P 2011 *J. Phys. B: At. Mol. Opt. Phys.* **44** 154011
[5] Patsch S, Reich D M, Raimond J-M, Brune M, Gleyzes S and Koch C P 2018 *Phys. Rev.* A **97** 053418
[6] Sørensen J J W *et al* 2016 *Nature* **532** 210
[7] Poyatos J F, Cirac J I and Zoller P 1996 *Phys. Rev. Lett.* **77** 4728
[8] Kraus B, Büchler H P, Diehl S, Kantian A, Micheli A and Zoller P 2008 *Phys. Rev.* A **78** 042307
[9] Verstraete F, Wolf M M and Cirac J I 2009 *Nat. Phys.* **5** 633
[10] Plenio M B, Huelga S F, Beige A and Knight P L 1999 *Phys. Rev.* A **59** 2468
[11] Benatti F, Floreanini R and Piani M 2003 *Phys. Rev. Lett.* **91** 070402
[12] Vacanti G and Beige A 2009 *New J. Phys.* **11** 083008
[13] Wolf A, Chiara G D, Kajari E, Lutz E and Morigi G 2011 *Europhys. Lett.* **95** 60008
[14] Gonzalez-Tudela A, Martin-Cano D, Moreno E, Martin-Moreno L, Tejedor C and Garcia-Vidal F J 2011 *Phys. Rev. Lett.* **106** 020501
[15] Cho J, Bose S and Kim M S 2011 *Phys. Rev. Lett.* **106** 020504
[16] Kastoryano M J, Reiter F and Sørensen A S 2011 *Phys. Rev. Lett.* **106** 090502
[17] Rao Bhaktavatsala D D and Mølmer K 2013 *Phys. Rev. Lett.* **111** 033606
[18] Habibian H, Zippilli S, Illuminati F and Morigi G 2014 *Phys. Rev.* A **89** 023832

[6] Typically of the order of one hundred propagations are necessary to converge the optimization.

[19] Taketani B G, Fogarty T, Kajari E, Busch T and Morigi G 2014 *Phys. Rev.* A **90** 012312
[20] Bentley C D B, Carvalho A R R, Kielpinski D and Hope J J 2014 *Phys. Rev. Lett.* **113** 040501
[21] Morigi G, Eschner J, Cormick C, Lin Y, Leibfried D and Wineland D J 2015 *Phys. Rev. Lett.* **115** 200502
[22] Aron C, Kulkarni M and Türeci H E 2016 *Phys. Rev.* X **6** 011032
[23] Reiter F, Reeb D and Sørensen A S 2016 *Phys. Rev. Lett.* **117** 040501
[24] Cormick C and Morigi G 2012 *Phys. Rev. Lett.* **109** 053003
[25] Diehl S, Micheli A, Kantian A, Kraus B, Büchler H-P and Zoller P 2008 *Nat. Phys.* **4** 878
[26] Habibian H, Winter A, Paganelli S, Rieger H and Morigi G 2013 *Phys. Rev. Lett.* **110** 075304
[27] Pastawski F, Clemente L and Cirac J I 2011 *Phys. Rev.* A **83** 012304
[28] Mirrahimi M, Leghtas Z, Albert V V, Touzard S, Schoelkopf R J, Jiang L and Devoret M H 2014 *New J. Phys.* **16** 045014
[29] Reiter F, Sørensen A S, Zoller P and Muschik C 2017 *Nat. Commun.* **8** 1822
[30] Kienzler D, Lo H-Y, Keitch B, de Clercq L, Leupold F, Lindenfelser F, Marinelli M, Negnevitsky V and Home J 2014 *Science* **347** 53
[31] Krauter H, Muschik C A, Jensen K, Wasilewski W, Petersen J M, Cirac J I and Polzik E S 2011 *Phys. Rev. Lett.* **107** 080503
[32] Lin Y, Gaebler J, Reiter F, Tan T, Bowler R, Sørensen A, Leibfried D and Wineland D 2013 *Nature* **504** 415
[33] Shankar S, Hatridge M, Leghtas Z, Sliwa K, Narla A, Vool U, Girvin S M, Frunzio L, Mirrahimi M and Devoret M H 2013 *Nature* **504** 419
[34] Kimchi-Schwartz M E, Martin L, Flurin E, Aron C, Kulkarni M, Tureci H E and Siddiqi I 2016 *Phys. Rev. Lett.* **116** 240503
[35] Syassen N, Bauer D M, Lettner M, Volz T, Dietze D, García-Ripoll J J, Cirac J I, Rempe G and Dürr S 2008 *Science* **320** 1329
[36] Schindler P, Müller M, Nigg D, Barreiro J T, Martinez E A, Hennrich M, Monz T, Diehl S, Zoller P and Blatt R 2013 *Nat. Phys.* **9** 361
[37] Barreiro J T, Müller M, Schindler P, Nigg D, Monz T, Chwalla M, Hennrich M, Roos C F, Zoller P and Blatt R 2011 *Nature* **470** 486
[38] Sobel'man I I 1972 *Introduction to the Theory of Atomic Spectra* (Oxford: Pergamon)
[39] Woodgate G K 1999 *Elementary Atomic Structure* (Oxford: Oxford University Press)
[40] Gardiner C W and Zoller P 2004 *Quantum Noise: A Handbook of Markovian and Non-Markovian Quantum Stochastic Methods with Applications to Quantum Optics* (*Springer Series in Synergetics* vol 56) (Berlin: Springer)
[41] Reiter F and Sørensen A S 2012 *Phys. Rev.* A **85** 032111
[42] Ozeri R *et al* 2007 *Phys. Rev.* A **75** 042329
[43] Johnson S G 2014 The nlopt nonlinear-optimization package
[44] Rowan T H 1990 Functional stability analysis of numerical algorithms *PhD Thesis* University of Texas at Austin
[45] Gaebler J P *et al* 2016 *Phys. Rev. Lett.* **117** 060505
[46] Goetz R E, Merkel M, Karamatskou A, Santra R and Koch C P 2016 *Phys. Rev.* A **94** 023420
[47] Monz T, Schindler P, Barreiro J T, Chwalla M, Nigg D, Coish W A, Harlander M, Hänsel W, Hennrich M and Blatt R 2011 *Phys. Rev. Lett.* **106** 130506
[48] Kraus B, Büchler H P, Diehl S, Kantian A, Micheli A and Zoller P 2008 *Phys. Rev.* A **78** 042307
[49] Albert V V 2017 Lindbladians with multiple steady states: theory and applications *PhD Thesis* Yale University
[50] Doucet E, Reiter F, Ranzani L and Kamal A 2018 arXiv:1810.03631
[51] de Vega I and Alonso D 2017 *Rev. Mod. Phys.* **89** 015001
[52] Reich D M, Katz N and Koch C P 2015 *Sci. Rep.* **5** 12430
[53] Huelga S F, Rivas A and Plenio M B 2012 *Phys. Rev. Lett.* **108** 160402